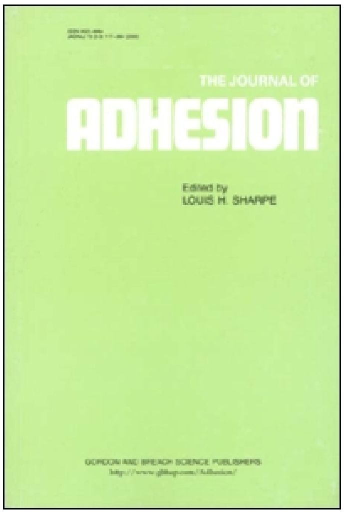

The Journal of Adhesion
Publication details, including instructions for authors and subscription information:
http://www.informaworld.com/smpp/title~content=t713453635

Epoxy Infiltration into Nanoporous Aluminum Oxide

D. Arayasantiparb[a]; S. McKnight[b]; M. Libera[a]
[a] Department of Chemical, Biochemical and Materials Engineering, Stevens Institute of Technology, Hoboken, New Jersey, USA [b] Army Research Laboratory, Aberdeen Proving Ground, Maryland, USA

To cite this Article Arayasantiparb, D. , McKnight, S. and Libera, M.(2001) 'Epoxy Infiltration into Nanoporous Aluminum Oxide', The Journal of Adhesion, 76: 4, 353 — 370

To link to this Article: DOI: 10.1080/00218460108030726

URL: http://dx.doi.org/10.1080/00218460108030726

The Journal of Adhesion, 76:353 - 370, 2001

0021-8464/01 $12.00 + .00

Epoxy Infiltration into Nanoporous Aluminum Oxide

D. ARAYASANTIPARB[a], S. McKNIGHT[b], and M. LIBERA[a]

[a]*Stevens Institute of Technology, Department of Chemical, Biochemical and Materials Engineering, Hoboken, New Jersey, USA;*
[b]*Army Research Laboratory, Aberdeen Proving Ground, Maryland, USA*

(Received 9 November 2000; in final form 22 March 2001)

This research uses spatially-resolved electron energy-loss spectroscopy (EELS) in a scanning transmission electron microscope (STEM) to study epoxy infiltration into a nanoporous aluminum surface oxide. Imaging by scanning electron microscopy (SEM) shows that the oxide surface of an as-anodized aluminum wire consists of columnar nanopores with diameters ranging from approximately 5 - 150 nm. Anodized wires were embedded in a 100 g : 28 g mixture of DGEBA (diglycidyl ether of bisphenol-A) resin and PACM20 (bis(p-aminocyclohexyl)methane) curing agent followed by a two-step cure. Electron-transparent sections were cut by ultramicrotomy. Spatially-resolved carbon and oxygen EELS profiles from the oxide are anti-correlated indicating that oxide pore walls are separated by pore interiors containing epoxy. Spatially-resolved low-loss spectral data are transformed into a measure of apparent specimen thickness. Comparisons of such data with simulations based on experimentally derived oxide topologies indicate that the pores are fully filled.

Keywords: Electron energy-loss spectroscopy; Nanoporous aluminum oxide; DGEBA; PACM20; Interphase; Electron microscopy

---

This work was supported by the Army Research Office (grants DAAG-55-98-1-0150 and DAAG55-97-1-0137) and a Royal Thai fellowship. The authors thank Dr. K. Sheppard of Stevens Institute for his help with the aluminum anodization. Thanks are also due to Dr. S. Wentworth and Dr. W. Zukas, formerly of the Army Research Laboratory (Watertown, MA) for their early involvement in this research.

Address correspondence to M. Libera, Stevens Institute of Technology, Department of Chemical, Biochemical, and Materials Engineering, Castle Point of Hudson, Hoboken, NJ 07030, USA. E-mail: mlibera@stevens-tech.edu

INTRODUCTION

The native oxide structure found on the surface of aluminum by itself does not promote long-term adhesion to polymeric adhesives [1–8]. Several processes have therefore been developed to produce more effective oxide structures on aluminum surfaces. Among these are acid etches, anodizing treatments, and plasma sprayed coatings [3, 9–17].

The structure of such oxides and the polymer-oxide interphase have been widely studied using a number of analytical techniques [1, 8, 9, 18–25]. Microporosity and microroughness of surface oxides have been previously observed. The interaction of the polymer with these porous surfaces can control the joint strength, toughness, and durability. Furthermore, a porous oxide filled with polymer adhesive in a joint may provide a region of intermediate modulus that enhances joint performance due to a desirable stress distribution in the interphase [5]. Thus, obtaining a polymer-filled porous oxide structure can significantly influence the structural integrity of bonded aluminum joints.

Many excellent electron micrographs of surface oxides have been obtained and are available in the literature [8, 26–30]. For example, the microporous structure due to phosphoric acid anodization (PAA) has been examined in detail using SEM [8, 31]. These previous efforts have revealed that the PAA surface oxide is approximately 0.5 μm thick with a honeycomb-like structure [8]. The pores range in diameter from about 40–120 nm depending on the anodizing conditions. There is evidence that at least some epoxy infiltrates this porous structure as one would anticipate, but the extent of this filling has not been fully quantified [32].

This work uses high-spatial-resolution electron-scattering methods to characterize in detail the nanoporous oxide structure of a PAA-treated aluminum surface and the filling of this structure by a model epoxy adhesive. The as-anodized surface is studied using a field-emission digital scanning electron microscope (FEG-SEM). The extent of pore filling is assessed using spatially-resolved electron energy-loss spectroscopy (EELS) in a scanning transmission electron microscope (STEM) [33]. Energy-loss spectroscopy is particularly well suited for studying materials containing light elements such as carbon and oxygen. In addition, the inelastically scattered signal can be used to quantify the specimen thickness. The results confirm that nanoporous oxides grown by PAA of an aluminum surface are indeed fully filled by a DGEBA/PACM20 epoxy.

EXPERIMENTAL PROCEDURE

A 125-μm diameter aluminum wire (Aluminum-1199, California Fine Wire Company) was annealed in an ambient air atmosphere using a Rapid Temp Furnace at 400°C for 4 hours. This annealing procedure was performed to minimize any residual stress that may result from the wire drawing process. The annealing facilitated the TEM specimen preparation process. The wire was cooled overnight and kept in an anhydrous atmosphere until it was anodized. Lengths of annealed wire (10 cm) were phosphoric acid anodized in accordance with SAE Aerospace Recommended Practice 1524 Rev A [34]. After anodizing, the wire was dried in an anhydrous oven at 80°C and cooled in an anhydrous atmosphere for approximately 30 minutes prior to embedding in epoxy.

This experiment used DGEBA (diglycidyl ether of bisphenol-A, Shell EPON 828®) as the epoxy resin and PACM20® (bis(p-aminocyclohexyl)methane, Air Products) as the curing agent mixed in stoichiometric amounts (100 g DGEBA: 28 g PACM20). The mixture was poured into a 1 × 0.5 × 0.5 cm rectangular silicone mold containing a single, straight, anodized aluminum wire. The epoxy was cured at 80°C for 2 hours and post-cured at 160°C for 2 hours. Differential scanning calorimetry (DSC) confirmed that this procedure led to a degree of cure exceeding 95%.

A portion of the anodized aluminum wire was retained for imaging the as-anodized surface. Such imaging was performed using a LEO 982 field-emission SEM operated at 10 keV with 10–15° tilt. There was insufficient charging of the specimen under these electron-irradiation conditions to necessitate coating with a conductive layer of carbon.

Epoxy-embedded specimens were cut by ultramicrotomy using a Riechart Ultracut E microtome at room temperature to produce electron-transparent cross sections. The specimens were cut perpendicular to the aluminum wire to expose a cross-section of the oxide. Cut sections were collected on 300-mesh TEM copper grids covered by a holey carbon film. TEM and STEM were performed using a 200 keV

Philips CM20 microscope. This instrument was equipped with a Schottky field emission gun (FEG) source whose high brightness enabled the formation of finely focused electron probes (~1–3 nm full-width at half-maximum, FWHM) with sufficient current (0.1–3 nA) to do meaningful scattering experiments at high spatial resolution [35]. Electron energy-loss spectroscopy (EELS) was done both in the low-loss and core-loss spectral regions using a post-column Gatan model 666 parallel spectrometer. Digital control of the microscope combined with digital image and spectral acquisition was provided by an EmiSpec Vision system [36]. All experiments were done at −134°C using a Gatan single-tilt cryostage to minimize hydrocarbon contamination and specimen-heating effects.

Core-loss electron energy-loss spectra were collected with a collection semi-angle of 16 mrad, a 1-sec dwell time, and an energy dispersion of 0.5 eV/channel over ranges of energy loss convenient to record the carbon-K edge (284 eV) and the oxygen-K edge (532 eV) simultaneously. The energy scales of these core-loss spectra were all calibrated after acquisition by aligning the 1 s-π^* pre-edge feature in the C-K edge to 284 eV. Standard background modeling and subtraction methods based on the AE^{-r} function, where E is the energy loss and A and r are fitting constants, were used [37].

Low-loss electron energy-loss spectra were collected with a dispersion of 0.2 eV/channel, a collection semi-angle of 10 mrad, and a 25-msec dwell time. Energy drift correction was done after acquisition by aligning the zero-loss peak to 0 eV.

Line profiles of spectra collected from the epoxy region consisted of 60 spectra collected from positions 5 nm apart. Line profiles of spectra collected from the oxide region consisted of 100 spectra from positions 3 nm apart.

RESULTS

Oxide Growth

The morphology of the aluminum surface oxide is described by Figure 1. This shows both SEM images of the as-anodized surface and cross-sectional TEM images of the oxide after embedding in epoxy for

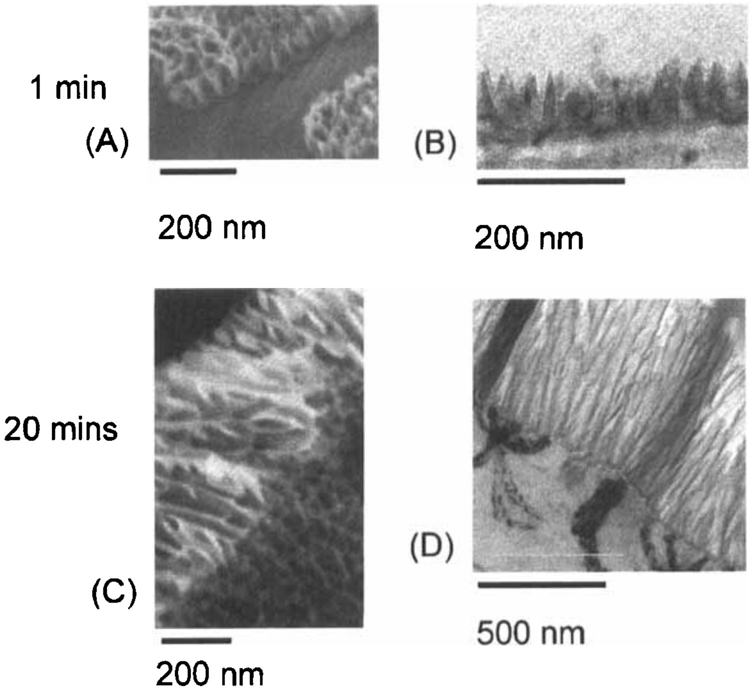

FIGURE 1 SEM (A,C) and TEM (B,D) images of the oxide after 1 min (A,B) and 20 mins (C,D) anodization times.

two different anodization-times (1 min and 20 mins). As expected, the thickness of the oxide layer increases with increasing anodization time from approximately 50 nm after 1 min of anodization to approximately 750 nm after 20 mins of anodization. Figure 2 presents SEM images of the oxide layer resulting from a 10-minute anodization process. Together, Figures 1 and 2 show that the oxide has a cellular morphology with elongated pores. The pore diameter (Fig. 2B) ranges from approximately 5 nm to 150 nm with a mean diameter of approximately 40 nm. The walls between adjacent pores range in thickness from 1 nm to 10 nm with a mean thickness of approximately 4 nm. These features are in agreement with earlier examinations of metal-coated PAA aluminum surfaces [8].

Figures 3A and 3B show a bright-field TEM image and a high-angle annular-dark-field (HAADF) STEM image of a cross-sectional specimen, respectively. The contrast is different in the epoxy and the

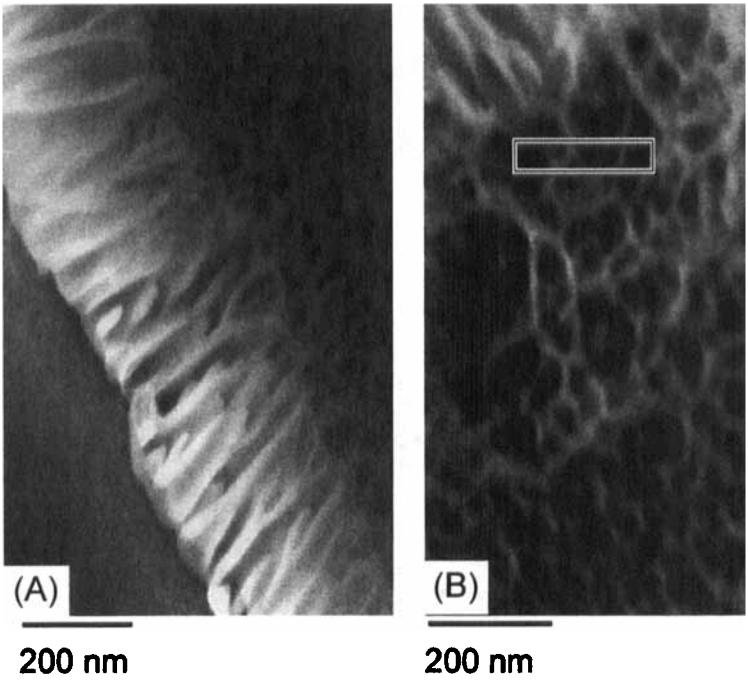

FIGURE 2 SEM micrographs showing (A) a side view and (B) a front view of an oxide layer formed by 10 mins of anodization. The white rectangle in (B) identifies a typical subimage used in simulations of TEM-based thickness profiles.

oxide, because of the nature of the two imaging processes used. Figure 3B shows dark contrast corresponding to a position where the aluminum metal delaminated at the Al/Al_2O_3 interface. This behavior occurred in some of the specimens studied here but did not appear to influence any of the energy-loss measurements made in the bulk epoxy or in the oxide. Figure 3B schematically illustrates the basic geometry for the two different spatially-resolved energy-loss profiling experiments. Type I profiles were collected along a line of points entirely in the bulk epoxy well away from the oxide. Type II profiles were collected along a line of points running entirely within the oxide at approximately one half of the distance across the Al_2O_3 layer. Both types of profiles were collected along directions parallel to the interface. Several profiles of each type were collected over distances ranging from approximately 300 nm to 1 μm.

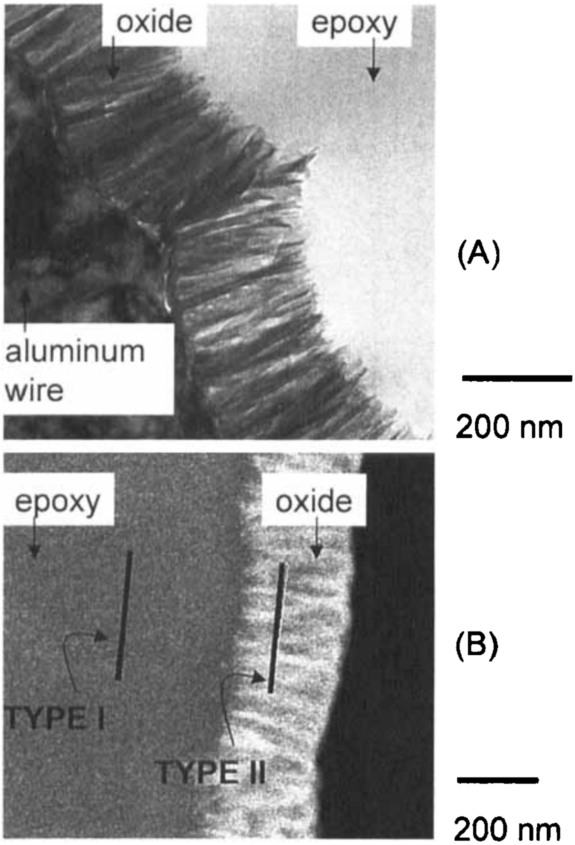

FIGURE 3 (A) Bright-field TEM image with epoxy-oxide-aluminum wire (B) HAADF STEM image schematically indicating the nature of Type I and Type II profiles.

Core-Loss Measurements

The results of core-loss profiling are presented in Figure 4. Figure 4A shows a typical Type I profile from the bulk epoxy of the background-subtracted carbon-K edge intensity normalized to the maximum intensity within this particular data set. This result shows that the carbon concentration is relatively uniform in the bulk. The root mean square (RMS) variation, $\Delta I_{N,C}$, can be determined by the expression:

$$\Delta I_{N,C} = \frac{\sum_{x=1}^{n} \sqrt{(I_{N,C} - \bar{I}_{N,C})^2}}{n} \tag{1}$$

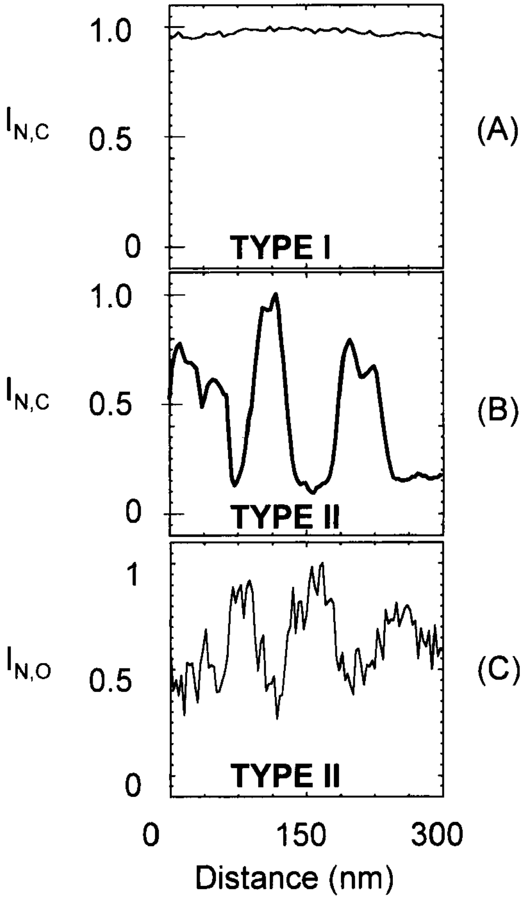

FIGURE 4 (A) Normalized carbon intensity from a Type I profile; (B) Normalized carbon intensity and (C) normalized oxygen intensity collected simultaneously from Type II profile.

where $I_{N,C}$ is the normalized carbon-K edge intensity at a given pixel position, x, $\bar{I}_{N,C}$ is the average normalized carbon intensity, and n is the total number of data points in the profile. For the data in Figure 4A, the RMS variation is 5.37×10^{-3}. Figures 4B and 4C show Type II carbon and oxygen profiles from the oxide. These show fluctuations as large as 50% or more of the maximum. The carbon and oxygen profiles are also inversely correlated. On average, where the carbon concentration drops, the oxygen concentration increases. The oxygen profile is somewhat noisier than the carbon profile due to fewer counts in the background-subtracted oxygen-K edge and the resulting higher shot noise.

Thickness Profiles

A relative thickness measurement in terms of total mean free path for inelastic electron scattering can be calculated based on the log-ratio formula [38, 39]:

$$\frac{t}{\lambda} = \ln\left(\frac{I_t}{I_0}\right) \tag{2}$$

where λ is a total mean free path (MFP) for inelastic scattering; t is the specimen thickness; I_t is the total intensity within the energy-loss spectrum; and I_0 is the intensity within the zero-loss peak. The MFP, λ, depends on the collection semi-angle, the atomic number, and the initial incident electron energy. It can be estimated from the following equations [38–40]:

$$\lambda = \frac{106F(E_0/E_m)}{\ln(2\beta E_0/E_m)} \tag{3}$$

$$F = \frac{1 + (E_0/1022)}{(1 + (E_0/511))^2} \tag{4}$$

$$E_m \approx 7.6Z^{0.36} \tag{5}$$

where λ is in nm; β is the collection semi-angle (10 mrad); E_0 is the incident energy (200 keV); E_m is the mean energy loss in eV; F is a relativistic factor; E_m is a function of the specimen composition (atomic %); and Z is the atomic number [37]. As shown by the chemical structure diagram in Figure 5, DGEBA/PACM20 epoxy consists of 38.3 at%C, 4.7 at%O, 2.0 at%N, and 55.0 at%H. Aluminum oxide (Al_2O_3) consists of 40 at%Al and 60 at%O. Calculated MFPs of epoxy, oxide, and vacuum are presented in Table I. These calculated values are consistent with the experimental data collected by Egerton and documented in Table II [41]. The experimental MFP of Al_2O_3 is less than that of the carbon measured

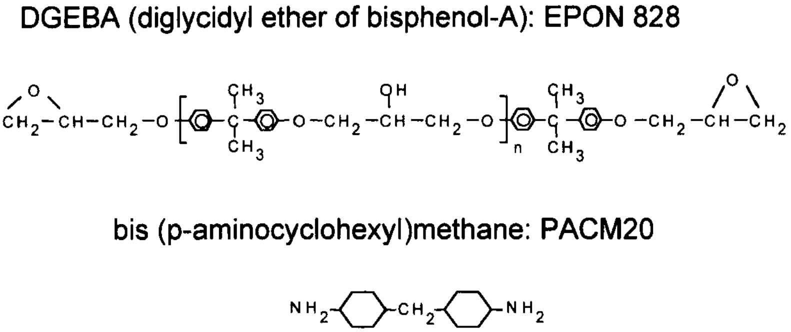

FIGURE 5 Molecular formulae of DGEBA (n = 0.2) and PACM20.

TABLE I Calculated total mean free paths for inelastic electron scattering characteristic of 200 keV electrons with 10 mrad collection semi-angle

Material	λ (*nm*)	$(t_{material}/\lambda_{material})$
Epoxy (DGEBA/PACM20)	180	0.222
Oxide (Al_2O_3)	138	0.290
Vacuum	∞	0

TABLE II Experimental total mean free paths for inelastic electron scattering characteristic of 100 keV electrons with 10 mrad collection semi-angle [41]

Material	λ (*nm*)
C thin film	116
Al_2O_3	106

with a 100 keV electron source. The difference of the two experimental MFPs is comparable with the difference of the calculated MFPs of Al_2O_3 and epoxy with a 200 keV electron source. One can generally expect the mean free path to increase with increasing incident electron energy.

The results of low-loss profiling are shown in Figure 6. These profiles describe the apparent specimen thickness, t_x, at each pixel position, x, in the scan normalized to the total mean free path for inelastic scattering at each pixel, λ_x. These (t_x/λ_x) data are derived from raw low-loss spectra using the well-established [37] formalism based on Eq. (2). Figure 6A shows the Type I (t_x/λ_x) profile collected from the bulk epoxy. This profile is almost constant with an RMS

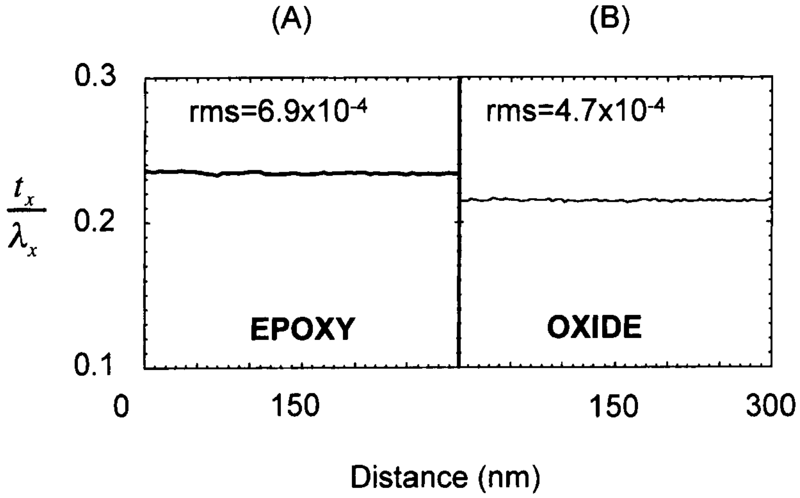

FIGURE 6 (A) Thickness profile from Type I profile, (B) Thickness profile from Type II profile.

variation, calculated using the algorithm in Eq. (1), of 6.9×10^{-4}. Figure 6B shows a (t_x/λ_x) profile from the oxide.

Again, the (t_x/λ_x) value is almost constant with an RMS variation of 4.7×10^{-4}. The average (t_x/λ_x) from the oxide is less than that from the bulk epoxy.

DISCUSSION

The phosphoric acid anodization treatment of aluminum produces a nanoporous surface oxide layer of controllable thickness. Figures 1A and 1B show an early stage of oxide layer formation. At the aluminum surface, there is a layer of dense oxide approximately 20–50 nm thick. Cone-shaped pores then appear as the oxide assumes a columnar morphology. The oxide layer becomes thicker with longer anodization time (Figs. 1C and 1D). The pores are highly columnar and extend in many cases through the entire oxide thickness. As illustrated by Figure 2, the pores assume a random arrangement in the two dimensions parallel to the aluminum substrate. These findings are generally consistent with several observations reported in the literature on similarly prepared aluminum oxides [10, 13, 19, 24, 28, 42, 43].

The question of whether the nanoporous oxide is filled without voids is addressed by the core-loss profiles shown in Figure 4. The carbon concentration is essentially constant in the bulk epoxy (Fig. 4A). These data suggest that the specimen is of relatively uniform thickness and, if there are fluctuations in local composition or density [44], they occur at approximately nanometer length scales that do not easily manifest themselves in the present experiments. The carbon concentration fluctuates dramatically in the profile from the oxide (Fig. 4B). Furthermore, the carbon concentration fluctuates inversely to that of oxygen (Fig. 4C). The fact that carbon is present in the oxide indicates that epoxy has at least partially infiltrated the nanoporous oxide [32]. The anti-correlated C—O fluctuation can be understood by recognizing that the thickness of oxide projected along the electron beam varies. The projected oxide thickness, t_{oxide}, is relatively high at positions where cell walls are aligned parallel to the electron beam. At these positions, the carbon concentration is relatively low. At adjacent regions where the electron beam predominantly traverses pores, one would expect the oxygen signal to drop. If the pores are filled by cured epoxy, the carbon signal would increase. Figures 4B and 4C precisely show this trend. One should recognize that the fluctuations in oxygen and carbon concentration do not in themselves give a measure of the pore wall or internal pore diameter, since these data are collected from two-dimensional projections of three-dimensional structures.

In contrast to the core-loss data, which scale with the amount of an element present at a particular position in the sample, the low-loss profiles provide data which measure the apparent specimen thickness, (t_x/λ_x), at each pixel position, x. The local apparent specimen thickness, (t_x/λ_x), can be described by:

$$\left(\frac{t_x}{\lambda_x}\right) = \left(\frac{t_{x,\text{oxide}}}{\lambda_{\text{oxide}}}\right) + \left(\frac{t_{x,\text{epoxy}}}{\lambda_{\text{epoxy}}}\right) + \left(\frac{t_{x,\text{vacuum}}}{\lambda_{\text{vacuum}}}\right) \qquad (6)$$

where $t_{x,\text{oxide}}$, $t_{x,\text{epoxy}}$, and $t_{x,\text{vacuum}}$ are the thicknesses of the oxide, epoxy, and vacuum at position x. The oxide has a complex three-dimensional topography such that the relative fractions of oxide, epoxy, and vacuum sampled at each pixel position vary. In addition, the mean free paths for scattering characteristic of Al_2O_3, epoxy, and vacuum differ (Tab. I). Consequently, (t_x/λ_x) varies as a function of lateral position over the specimen.

The question of whether all the pores are filled by epoxy is addressed by comparing the experimental (t_x/λ_x) thickness profiles (*e.g.*, Fig. 6B) with simulated profiles (Figs. 7A, 7B, 7C). The details of these simulations are described below. Briefly, they show that if a fraction of the pores are unfilled, there would be wide variations in the characteristic (t_x/λ_x) of the Type II profiles in the oxide. In contrast, very small fluctuations are observed experimentally in the Type II (t_x/λ_x) profiles. One can, thus, conclude that the pores are fully filled with no entrapped air (voids) in the porous oxide structure.

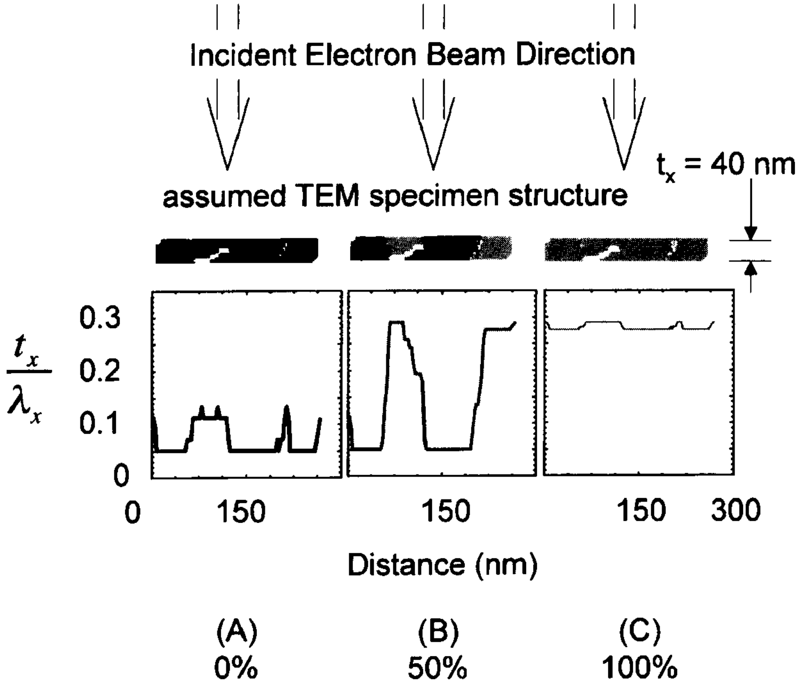

FIGURE 7 Simulation of apparent thickness as a function of position in a model nanoporous specimen with (A) unfilled, (B) 50%-filled, and (C) fully filled nanopores. In the assumed specimen structures, white = oxide, black = vacuum, and grey = epoxy.

The physical model used to simulate the oxide for Type II (t_x/λ_x) profiles is based on experimentally-derived data. Using the average (t_x/λ_x) value characteristic of the bulk epoxy together with the estimated mean free path, λ_{epoxy} (Tab. I), one can estimate that the epoxy thickness in the sample studied in Figure 6 is ~40 nm. The model assumes that the oxide portion of the specimen has this same thickness. A model oxide topography is chosen by extracting sub-images of the porous oxide from SEM images of oxides. An example is given by the white box inscribed on Figure 2B. The height of this box is 40 nm, corresponding to specimen thickness in the model, and the length is ~300 nm, corresponding to the lateral length over which the (t_x/λ_x) profile is simulated. After extracting the sub-image, the contrast is binarized, such that portions with white contrast above some threshold are defined as oxide, and the remaining portions below that threshold with black contrast are defined as vacuum. Digital image erosion methods [45] are used to make minor adjustments to the area fractions of the white and dark regions so that these are consistent with the average area fraction of oxide (0.08) given by the entire image in Figure 2B. Simulations were performed using a number of different sub-image-based oxide topographies as well as topographies based on arrays of nanopores defined by hexagonal patterns of oxide pore walls. The results of simulations using these various specimen topographies are all qualitatively similar, and the results of only one such simulation are presented here.

The apparent thickness, (t_x/λ_x), at each pixel position, x, in the model specimens is calculated by determining the partial thickness of oxide, epoxy, and vacuum $(t_{x,\text{oxide}}, t_{x,\text{epoxy}}, t_{x,\text{vacuum}})$ such that:

$$t_x = t_{x,\text{oxide}} + t_{x,\text{epoxy}} + t_{x,\text{vacuum}} = 40 \text{ nm}$$

For a given oxide topography $t_{x,\text{oxide}}$ is fixed. Different degrees of pore filling correspond to different relative contributions of $t_{x,\text{epoxy}}$ and $t_{x,\text{vacuum}}$ such that

$$t_{x,\text{epoxy}} + t_{x,\text{vacuum}} = 40 \text{ nm} - t_{x,\text{oxide}}.$$

A calculated value for (t_x/λ_x) at each pixel position can then be directly determined using Eq. (6) and the data in Table I.

Figure 7 presents the results of representative simulations for the specific oxide topography defined by the inset to Figure 2B where the pores are entirely unfilled (Fig. 7A), 50% filled (Fig. 7B), and entirely filled by epoxy (Fig. 7C). The fluctuations in the (t_x/λ_x) profiles characteristic of the unfilled and 50%-filled specimens are significant.

The RMS variation in (t_x/λ_x) is on the order of 10^{-2} to 10^{-1}. This is a consequence of the fact that any pores filled by vacuum do not contribute to (t_x/λ_x), because $\lambda_{x,\text{vacuum}}$ is infinite. There is, thus, substantial fluctuation in the (t_x/λ_x) profile where unfilled pores are positioned adjacent to filled pores or oxide pore walls. The RMS variation in (t_x/λ_x) for the fully-filled structure is of order 10^{-3}. As illustrated by Table I, the magnitudes of λ_{oxide} and λ_{epoxy} are comparable. The variations in the simulated (t_x/λ_x) profile for the filled structure are due to the small differences between these mean free paths as well as to the spatial variations in the distribution of oxide and epoxy in the model specimen. Again, while the quantitative nature of the various simulated profiles depends on the oxide topography assumed in the model, for a range of assumed topographies with pore diameters and wall thickness consistent with the image data of Figures 1–3, the profiles are qualitatively very similar.

The experimental (t_x/λ_x) profiles from the oxide (Fig. 6B) are clearly most similar to the (t_x/λ_x) simulations from the fully filled oxide (Fig. 7C). In particular, the RMS variation of (t_x/λ_x) in the experiment is of order 5×10^{-4}. While the exact value does not match identically the RMS variation from the specific simulation, the agreement is far better than when porosity is introduced into the model structure. If voids or air pockets are present in the nanopores, one would expect substantially more fluctuation in the (t_x/λ_x) than experimentally observed.

Clearly, the comparisons between the simulated and experimental data do not address the issue of whether individual pores are partially filled by epoxy. In such an event, one could consider whether a vacuum fraction of 5% or 10% would lead to variations significant enough to be distinguished experimentally from fluctuations in the oxide and epoxy distributions. One can plausibly argue against partial filling, however. If the changes in surface energy associated with wetting of the oxide is sufficient to overcome the entropic repulsion due to confinement of monomers or growing oligomers in the pores, one would expect the pores to be filled with epoxy. Palmese and

McCullough have shown [46–48] that the wetting of carbon fibers by the DGEBA/PACM20 system occurs well before the curing processes significantly affects the diffusive kinetics in this system. While the surface energies between an oxidized aluminum adherend and DGEBA/PACM20 (σ_{DGEBA/Al_2O_3}, σ_{PACM20/Al_2O_3}) are certainly different from each other, as well as from those between a carbon fiber adherend and these monomeric components, given the high surface energy between Al_2O_3 and air, one can expect that there would be a strong enthalpic driving force to wet the oxide within the nanopores.

CONCLUSIONS

This research has used field-emission scanning electron microscopy (FEG-SEM) together with spatially-resolved electron energy-loss spectroscopy (EELS) in a scanning transmission electron microscope (STEM) to characterize the nature of the nanoporous oxide-epoxy interphase in anodized aluminum-epoxy bond. Based on results of both core-loss and low-loss spectroscopy, coupled with simulations of spatially-resolved thickness profiles, this research concludes that the nanoporous oxide is fully filled with epoxy. This finding is consistent with the well-established idea that aluminum anodization enhances adhesive strength, since a fully-filled pore structure enhances both the total epoxy-adherend surface area and the degree of mechanical interlocking afforded by a highly porous interfacial structure. Furthermore, this work demonstrates the utility of high-resolution electron energy-loss spectroscopy to study the nanoscale chemistry of polymer-solid interphases.

References

[1] Ahearn, J. S., Davis, G. D., Sun, T. S. and Venables, J. D., In: *Adhesion Aspects of Polymeric Coatings*, Mittal, K. L. Ed. (Plenum Press, New York, 1983) pp. 281–299.

[2] Andrews, E. H. and King, N. E., In: *Polymer Surfaces*, Clark, D. T. and Feast, W. J. Eds. (John Wiley & Sons, NY, 1978), pp. 47–63.

[3] Arrowsmith, D. J., Moth, D. A. and Rose, S. P., *Intern. J. Adhesion and Adhesives* **12**(2), 67 (1992).

[4] Boerio, F. J., Davis, G. D., deVries, J. E., Miller, C. E., Mittal, K. L., Opila, R. L. and Yasuda, H. K., *Critical Reviews in Surface Chemistry* **3**(1), 81 (1993).

[5] Davies, R. J. and Ritchie, M. D., *J. Adhesion* **38**, 243 (1992).
[6] Kinloch, A. J., *J. Mate. Sci.* **15**, 2141-2166 (1980).
[7] Kinloch, A. J., In: *Materials in Aerospace: The First International Conference* (England Royal Aeronautical Society, London, England, 1986), pp. 279-289.
[8] Venables, J. D., *J. Mate. Sci.* **19**, 2431-2453 (1984).
[9] Ahearn, J. S. and Davis, G. D., *J. Adhesion* **28**, 75 (1989).
[10] Ahearn, J. S., Froede, C., Venables, J. D., Hopping, R. and Sun, T. S., *SAMPE Quarterly* **12**(1), 39 (1980).
[11] Davis, G. D., Whisnant, P. L., Shaffer, D. K., Groff, G. B. and Venables, J. D., *J. Adhesion Sci. Technol.* **9**(4), 527 (1995).
[12] Fourche, G., *Polymer Engineering and Science* **35**(12), 968 (1995).
[13] Li, A. P., Muller, F., Birner, A., Nielsch, K. and Gosele, U., *J. App. Physics* **84**(11), 6023 (1998).
[14] McNamara, D. K., Venables, J. D., Sun, T. S., Chen, J. M. and Hopping, R. L., In: *11th National SAMPE Technical Conference, New Horiz – Mater and Processes for the Eighties*, Boston, 1979), pp. 740-751.
[15] Sun, B. K. and O'Keefe, T. J., *Surface and Coatings Technology* **106**, 44 (1998).
[16] Turner, R. H., Segall, I., Boerio, F. J. and Davis, G. D., *J. Adhesion* **62**(1-4), 1 (1997).
[17] Zdunek, K., Mizera, J., Wiencek, P., Gebicki, W. and Mozdzonek, M., *Thin Solid Films* **343-344**, 324 (1999).
[18] Crompton, J. S., *J. Mater. Sci.* **24**, 1575-1581 (1989).
[19] Davis, G. D., Sun, T. S., Ahearn, J. S. and Venables, J. D., *J. Mater. Sci.* **17**(6), 1807-1818 (1982).
[20] Davis, G. D. and Venables, J. D., *Surface and Interface Analysis* **17**, 439 (1991).
[21] Hercules, D. M., In: *Characterization of Metal and Polymer Surfaces*, Lee, L.-H. Ed. (Academic Press, Inc., New York, 1977), pp. 399-430.
[22] Matienzo, L. J., Shah, T. K. and Venables, J. D., In: *15th National SAMPE Technical Conference: Vision in Materials for 2000*, Cincinnati, OH, 1983), pp. 604-616.
[23] Packham, D. E., Hine, P. J. and El Muddarris, S., In: *23rd Annual Conference on Adhesion and Adhesives*, Barking, England, 1986), p. 81.
[24] Sun, T. S., McNamara, D. K., Ahearn, J. S., Chen, J. M., Ditchek, B. and Venables, J. D., *Applications of Surface Science* **5**(4), 406 (1980).
[25] Van Ooij, W. J., *Surface Science* **68**, 1 (1977).
[26] Berbezier, I., Romand, M., Martin, J. M. and Cuntz, J. M., *J. Adhesion Sci. Technol.* **6**(7), 829 (1992).
[27] Bishopp, J. A., Smith, T., Thompson, G. E. and Wood, G. C., Allen, K.W., Ed. (*Elsevier Applied Science*, London, 1988).
[28] Drzal, L. T., Rich, M. J. and Drown, E. K., *ARO Final Report*, Contract No. DAAL03-91-0034, (1994).
[29] Nitschke, F., *J. Adhesion Sci. Technol.* **5**(9), 697 (1991).
[30] Venables, J. D., *J. Adhesion* **39**, 79 (1992).
[31] Davies, R. J. and Ritchie, M. D., In: *Conference on Adhesion and Adhesives*, Allen, K. W. Ed. Elsevier Applied Science, London, 1988).
[32] Brockmann, W., Hennemann, O. D., Kollek, H. and Matz, C., *Intern. J. Adhesion and Adhesives* **6**(3), 115-143 (1986).
[33] Siangchaew, K. and Libera, M., *Microscopy and Microanalysis* **3**, 530 (1997).
[34] ASTM Standard, D 3933-93 (1997).
[35] Libera, M., Smith, D. A., Tsung, L. and Eaglesham, D., *Ultramicroscopy* **52**, 564 (1993).
[36] http:www. Emispec.com.
[37] Egerton, R. F., *Electron Energy-Loss Spectroscopy in the Electron Microscope* (Plenum Press, New York and London, 1996), 2nd edition, pp. 301-307.

[38] Malis, T., Cheng, S. C. and Egerton, R. F., *Electron Microscopy Technique* **8**, 193 (1988).
[39] Yang, Y. Y. and Egerton, R. F. (1995) *Micron* **26**(1), 1 (1995).
[40] http://tpm.amc.anl.gov Tools/NTLambda.html.
[41] Egerton, R. F., In: *50th Ann. Proc. Electron Microsc. Soc. Amer* (San Francisco Press, San Francisco, 1992), pp. 1264-1265.
[42] Hennemann, O. D. and Brockmann, W., *Adhesion* **12**, 297 (1981).
[43] Vanden Berg, R. V., *Surface Preparation and Finishes for Metals.* (McGraw-Hill Book Company, New York, 1971), pp. 228-245.
[44] Yim, H., Kent, M., McNamara, W. F., Ivkov, R., Satija, S. and Majewski, J., *Macromolecules* **32**(33), 7932-7938 (1999).
[45] Russ, J. C., In: *Proc. 51st Annual Meeting of the Microscopy Society of America* (San Francisco Press, San Francisco, CA, 1993), pp. 536-537.
[46] Palmese, G. R., Origin and Influence of Interphase Material Property Gradients in Thermosetting Composites, In: *Chemical Engineering*, University of Delaware (1991).
[47] Palmese, G. R. and McCullough, R. L., *J. Appl. Polym. Sci.* **46**, 1863 (1992).
[48] Palmese, G. R. and McCllough, R. L., *Composites-Part A: Applied Science and Manufacturing* **30**(1), 3 (1999).